Computers and Fluids 141 (2016) 105–115

Contents lists available at ScienceDirect

Computers and Fluids

journal homepage: www.elsevier.com/locate/compfluid

A stabilized nodally integrated meshfree formulation for fully coupled hydro-mechanical analysis of fluid-saturated porous media

Haoyan Wei, Jiun-Shyan Chen*, Michael Hillman

Department of Structural Engineering, University of California, San Diego, 9500 Gilman Drive, La Jolla, CA 92093, United States

ARTICLE INFO

Article history:
Received 5 September 2015
Revised 23 September 2015
Accepted 9 November 2015
Available online 19 November 2015

Keywords:
Meshfree methods
Reproducing Kernel Particle Method
Stabilized conforming nodal integration
Pressure projection
Fluid-saturated porous media
Coupled hydro-mechanical analysis

ABSTRACT

Numerical modeling of reservoirs with low permeability or under undrained conditions often suffers from spurious fluid pressure oscillations due to the improper construction of approximation spaces. To address this issue, a fully coupled, stabilized meshfree formulation is developed based on a fluid pressure projection method, in which an additional stabilization term is added to the variational equation to correct the deficiency of the equal-order u–p reproducing kernel approximation. The projection scheme is formulated under the framework of the stabilized conforming nodal integration which enables a significant enhancement of the computational efficiency and accuracy, and the spurious low-energy modes of nodal integration are also eliminated. The effectiveness of the proposed stabilized meshfree formulation is demonstrated by solving several benchmark problems.

1. Introduction

The coupled hydro-mechanical phenomenon in fluid-saturated porous media is of great importance in a number of geotechnical engineering applications from the safety analysis of slopes and dams to the design of underground storage of toxic or radioactive waste, as well as the stimulation in low-permeable gas and oil reservoirs, to name a few. In order to achieve reliable and efficient modeling of such complicated physical processes, various computational poromechanical formulations based on the Finite Element Method (FEM) or the meshfree method have been developed over the years.

Meshfree methods [1–4] can overcome several drawbacks that are inherently associated with FEM. For instance, the time-consuming mesh generation process and the computational errors induced by distorted or low quality meshes in FEM can be avoided in meshfree methods [3]. Additionally, with the flexibility of controlling the order of smoothness, continuity and locality, the meshfree approximation offers exceptional benefits for solving problems with moving discontinuities such as crack propagation [5–7] and problems with high order differentiation such as shear band formation via gradient plasticity or damage material models [8,9]. Several coupled meshfree formulations have been proposed for the porous media modeling, including the Element-Free Galerkin (EFG) method [10–15], the Radial Point Interpolation Method (RPIM) [16–18] and the Smoothed Particle Hydrodynamics (SPH) method [19], which have shown the advantages of meshfree methods in producing more accurate solutions for coupled problems over the standard FEM. Recently, the Reproducing Kernel Particle Method (RKPM) has been extended to solve the poromechanics problems based on a sequentially coupled scheme to ensure the stability of the staggered iteration procedure used in between different solvers [20].

Although in previous research work the promising capabilities of meshfree methods for solving geomechanics problems have been demonstrated [10–20], some critical numerical issues remain. One of such challenges is the spurious fluid pressure oscillations when modeling reservoirs with low permeability or under undrained conditions. This is a consequence of violation of the Babuska–Brezzi inf-sup condition [21–23]. Some earlier works on inf-sup stable mixed formulation have been proposed, where different orders of interpolations are chosen for the spatial discretization of the solid displacement u and the fluid pressure p [24,25]. However, these mixed-order interpolations complicate the implementation and are usually computationally expensive due to the requirement of extra degrees of freedom and high order domain integration schemes. On the other hand, the equal-order approximation is in practice quite attractive because of its simplicity and efficiency for solving large-scale problems, especially for modeling fractured reservoirs [26]. To this end, various stabilization strategies have been proposed to achieve oscillation-free solutions with an equal-order u–p approximation, including the fractional step algorithm [27,28], the Galerkin Least Squares formulation [29], the fluid pressure Laplacian method [30], and the fluid pressure projection method [31–34], etc. Among these different stabilization approaches, the pressure

* Corresponding author. Tel.: +1 818 486 9538.
E-mail address: js-chen@ucsd.edu (J.-S. Chen).

http://dx.doi.org/10.1016/j.compfluid.2015.11.002
0045-7930/

projection based method has been proposed for nearly incompressible finite elasticity [35–37], stokes flow [38,39] and poromechanics [31–34]. Compared to other stabilization techniques, the pressure projection method has several appealing features such as the avoidance of stress-recovery techniques or high-order derivatives of shape functions commonly used in the Petrov–Galerkin type methods [29], and also the stability property of the time-integration scheme is not affected, unlike the fractional step algorithm [27,28].

While most of the research work on stabilization for poromechanics problems has been focused on FEM, very few attempts have been made to address this issue in the context of meshfree methods. The work by Hua [14] showed that the fluid pressure oscillation can be avoided by adjusting the numbers of u and p field nodes in the EFG method, however, it is not clear how an optimal distribution of the nodes can be designed for general cases. The stabilized Petrov–Galerkin formulation has been employed by Xie et al. [20] to eliminate the pressure oscillation in the RKPM method; however, this method results in a non-symmetric system matrix and requires calculation of high-order derivatives of meshfree shape functions which is time consuming.

Another numerical issue in the meshfree modeling for poromechanical problems is the domain integration technique. While Gauss quadrature rule has been commonly used in meshfree methods for the domain integration of weak form, considerable integration errors could be generated since the meshfree approximation functions are in general of rational type with often complicated overlapping support structures [40], and a very high order quadrature rule has to be adopted to achieve integration accuracy, which is computationally expensive. Methods such as direct nodal integration, on the other hand, could lead to instability due to rank deficiency, and also yields poor accuracy and low convergence rates [41]. To simultaneously attain efficiency, accuracy and also stability in nodal integration, the stabilized conforming nodal integration (SCNI) method has been proposed by Chen et al. [42,43] which achieves high accuracy and optimal convergence associated with approximation spaces with linear completeness. The generalization of SCNI for 2^{nd} order bases [44] and for arbitrary order bases by a variational consistency condition [45] have also been proposed. Although integration techniques have been studied intensively, research on proper integration techniques for mixed formulations is rare and therefore deserves investigation.

In this paper, we propose a stabilized RKPM formulation for the fully coupled hydro-mechanical analysis of fluid saturated geomaterials. The fluid pressure projection method is formulated within the SCNI framework, in which an L_2 projection operator is defined locally in each nodal representative domain and an associated stabilization term is added to the variational equation to correct the deficiency of the equal-order u–p approximation. Furthermore, the projection scheme is shown to be compatible with SCNI with enhanced stabilization, enabling a significant enhancement of computational accuracy and efficiency.

The arrangement of this paper is as follows. After a brief description of the poromechanics theory in Section 2, the reproducing kernel mixed formulation is given in Section 3. The fluid pressure projection based RKPM formulation is then introduced under the SCNI framework in Section 4, and several benchmark problems are analyzed in Section 5 to demonstrate the effectiveness of the proposed stabilized meshfree formulation. Concluding remarks are given in Section 6.

2. Governing equations of fluid-saturated porous media

2.1. Strong form

Consider a porous medium occupying a domain Ω with boundary Γ as shown in Fig. 1. According to the poromechanics theory [46,47], all phases are present at every point at the same time. As a result, the equations governing the deformation of a porous solid saturated with fluid can be derived from the principles of momentum and mass conservation of the mixture, which can be expressed as

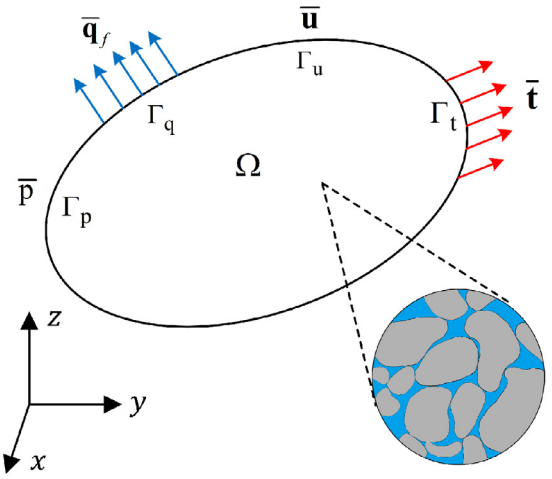

Fig. 1. A fluid saturated porous medium occupying the domain Ω with boundary Γ.

$$\nabla \cdot \left(\boldsymbol{\sigma}'' - \alpha p \mathbf{I}\right) + \rho \mathbf{g} = \mathbf{0} \tag{1}$$

$$\alpha \nabla \cdot \frac{\partial \mathbf{u}}{\partial t} + \nabla \cdot \mathbf{q}_f + \frac{1}{Q}\frac{\partial p}{\partial t} = 0 \tag{2}$$

along with the following boundary conditions:

$$\mathbf{u} = \bar{\mathbf{u}} \quad \text{on} \quad \Gamma_u \tag{3}$$

$$\mathbf{n}_\Gamma \cdot \left(\boldsymbol{\sigma}'' - \alpha p \mathbf{I}\right) = \bar{\mathbf{t}} \quad \text{on} \quad \Gamma_t \tag{4}$$

$$p = \bar{p} \quad \text{on} \quad \Gamma_p \tag{5}$$

$$-\mathbf{n}_\Gamma \cdot \mathbf{k}_f \cdot \nabla \mathrm{p} = \mathbf{n}_\Gamma \cdot \bar{\mathbf{q}}_f \quad \text{on} \quad \Gamma_q \tag{6}$$

and the initial conditions at time $t = 0$:

$$\mathbf{u} = \mathbf{u}_0, \quad p = p_0 \tag{7}$$

where $\mathbf{u}$ and p represent the solid displacement and the fluid pressure, respectively; $\boldsymbol{\sigma}''$ is the effective stress, with the sign convention for tensile effective stress $\boldsymbol{\sigma}''$ and compressive fluid pressure p as positive; $\mathbf{I}$ is a second-order identity tensor; $\rho = n_f\rho_f + (1-n_f)\rho_s$ is the averaged mass density, in which n_f is the volume fraction of the fluid phase, often referred to as porosity, and ρ_s and ρ_f are the mass densities of the solid and fluid phases, respectively; $\mathbf{g}$ is the gravity acceleration; the fluid storage coefficient is defined as $1/Q = (\alpha - n_f)/K_s + n_f/K_f$, in which Q is the compressibility modulus, $\alpha = 1 - K/K_s$ is Biot's coefficient, K_s and K_f are the averaged bulk modulus of the solid grains and fluid, respectively, and $K = E/[3(1-2\nu)]$ is the bulk modulus of the overall solid skeleton, where E and ν are Young's modulus and Poisson's ratio of the dry porous matrix, respectively; $\mathbf{q}_f$ is the fluid flow flux relative to the solid skeleton; $\mathbf{n}_\Gamma$ is the unit outer normal vector of the boundary Γ, Γ_u and Γ_p are the essential boundaries with imposed solid displacement and fluid pressure, respectively, and Γ_t and Γ_q are the natural boundaries with imposed traction and fluid outflow flux, respectively, where $\Gamma_u \cap \Gamma_t = \Gamma_p \cap \Gamma_q = \emptyset$ and $\Gamma_u \cup \Gamma_t = \Gamma_p \cup \Gamma_q = \Gamma$; and the effective stress $\boldsymbol{\sigma}''$ can be defined through the constitutive relationship as follows:

$$\boldsymbol{\sigma}'' = \mathbf{C} : \boldsymbol{\varepsilon} \tag{8}$$

where $\mathbf{C}$ is the elastic modulus tensor of the solid skeleton, and $\boldsymbol{\varepsilon}$ is the strain tensor, defined as the symmetric part of the solid

displacement gradient:

$$\boldsymbol{\varepsilon} = \nabla^s \mathbf{u} = \frac{1}{2}\left(\nabla \mathbf{u} + \nabla \mathbf{u}^{\mathrm{T}}\right) \tag{9}$$

The barotropic fluid characterized by the fluid pressure field p is considered in the following discussions, and the fluid flow $\mathbf{q}_f$ is then defined by the Darcy's law:

$$\mathbf{q}_f = -\mathbf{k}_f \cdot \left(\nabla \mathrm{p} - \rho_f \mathbf{g}\right) \tag{10}$$

where $\mathbf{k}_f = \mathbf{k}_h/\gamma_f$ is the permeability tensor, in which $\mathbf{k}_h$ is the hydraulic conductivity tensor and γ_f is the specific weight of the fluid. Note that the permeability tensor can be alternatively expressed as the ratio of the so-called intrinsic permeability tensor to the dynamic viscosity, and in general it can evolve with the change of void ratio, micro-cracks density and distribution, etc. For simplicity, here $\mathbf{k}_f$ is considered to be constant and isotropic, i.e., $\mathbf{k}_f = k_f \mathbf{I}$. Substituting Eq. (10) into Eq. (2), and combining with Eq. (1), the classical u– p form of the poromechanics governing equations can be obtained, which are employed in the present study.

2.2. Weak form

To arrive at the weak form, two spaces of trial functions for both solid displacement and fluid pressure fields in d-dimension are defined as

$$S_u = \{\mathbf{u} : \Omega \to \mathbb{R}^d | \mathbf{u} \in [\mathbb{H}^1]^d, \mathbf{u} = \bar{\mathbf{u}} \text{ on } \Gamma_u\} \tag{11}$$

$$S_p = \left\{p : \Omega \to \mathbb{R} | p \in \mathbb{H}^1, p = \bar{p} \text{ on } \Gamma_p\right\} \tag{12}$$

The corresponding spaces of test functions are

$$V_u = \left\{\boldsymbol{\eta} : \Omega \to \mathbb{R}^d \middle| \boldsymbol{\eta} \in \left[\mathbb{H}^1\right]^d, \boldsymbol{\eta} = \mathbf{0} \text{ on } \Gamma_u\right\} \tag{13}$$

$$V_p = \left\{\psi : \Omega \to \mathbb{R} | \psi \in \mathbb{H}^1, \psi = 0 \text{ on } \Gamma_p\right\} \tag{14}$$

The weak form statement of the problem in Section 2.1 is then to find $(\mathbf{u}, p) \in S_u \times S_p$ such that for all $(\boldsymbol{\eta}, \psi) \in V_u \times V_p$,

$$\begin{aligned}\mathscr{L}_1(\boldsymbol{\eta}; \mathbf{u}, p) \equiv & \int_\Omega \left(\nabla^s \boldsymbol{\eta} : \boldsymbol{\sigma}'' - \alpha p \nabla \cdot \boldsymbol{\eta}\right) \mathrm{d}\mathbf{x} \\ & - \int_{\Gamma_t} \boldsymbol{\eta} \cdot \bar{\mathbf{t}} \mathrm{d}\mathbf{s} - \int_\Omega \boldsymbol{\eta} \cdot \rho \mathbf{g} \mathrm{d}\mathbf{x} = 0\end{aligned} \tag{15}$$

$$\begin{aligned}\mathscr{L}_2(\psi; \mathbf{u}, p) \equiv & \int_\Omega \alpha \psi \nabla \cdot \frac{\partial \mathbf{u}}{\partial t} \mathrm{d}\mathbf{x} + \int_\Omega \psi \frac{1}{Q} \frac{\partial p}{\partial t} \mathrm{d}\mathbf{x} \\ & + \int_\Omega \nabla \psi \cdot \mathbf{k}_f \cdot \nabla p \mathrm{d}\mathbf{x} + \int_{\Gamma_q} \psi \mathbf{n}_\Gamma \cdot \bar{\mathbf{q}}_f \mathrm{d}\mathbf{s} = 0\end{aligned} \tag{16}$$

3. Reproducing kernel mixed formulation

3.1. Reproducing kernel approximation

Let $\{\mathbf{x}_I, \mathbf{x}_I \in \Omega\}_{I=1}^{NP}$ be a set of nodes in the domain, $\mathbf{x}_I$ is the position vector of node I, and NP is the total number of nodes. The discrete reproducing kernel approximation [2,3] of a function $f(\mathbf{x})$ in the domain Ω is as follows:

$$f^h(\mathbf{x}) = \sum_{I=1}^{NP} N_I(\mathbf{x}) f_I \tag{17}$$

where f_I is the coefficient, and $N_I(\mathbf{x})$ is the n^{th} order reproducing kernel shape function expressed as

$$N_I(\mathbf{x}) = C(\mathbf{x}; \mathbf{x} - \mathbf{x}_I) \Phi_a(\mathbf{x} - \mathbf{x}_I) \tag{18}$$

in the above equation, $C(\mathbf{x}; \mathbf{x} - \mathbf{x}_I)$ is a correction function, and $\Phi_a(\mathbf{x} - \mathbf{x}_I)$ is the kernel function that controls the locality and smoothness of the approximation, which is chosen to be the cubic spline function in the present study:

$$\Phi_a(\mathbf{x} - \mathbf{x}_I) = \begin{cases} 2/3 - 4s_I^2 + 4s_I^3 & \text{for} \quad 0 \le s_I \le 1/2 \\ 4/3 - 4s_I + 4s_I^2 - 4/3 s_I^3 & \text{for} \quad 1/2 < s_I \le 1 \\ 0 & \text{for} \quad s_I > 1 \end{cases} \tag{19}$$

where $s_I = \|\mathbf{x} - \mathbf{x}_I\|/a_I$, and a_I is the support size of node I. The correction function is defined as:

$$C(\mathbf{x}; \mathbf{x} - \mathbf{x}_I) = \mathbf{b}^{\mathrm{T}}(\mathbf{x}) \mathbf{H}(\mathbf{x} - \mathbf{x}_I) \tag{20}$$

in which $\mathbf{H}(\mathbf{x} - \mathbf{x}_I)$ is a vector consisting of n^{th} order monomial basis functions:

$$\mathbf{H}^{\mathrm{T}}(\mathbf{x} - \mathbf{x}_I) = [1,\ x - x_I,\ y - y_I,\ z - z_I,\ (x - x_I)^2,\ \cdots,\ (z - z_I)^n] \tag{21}$$

and $\mathbf{b}(\mathbf{x})$ is the coefficient vector to be determined from the following n^{th} order discrete reproducing conditions:

$$\sum_{I=1}^{NP} N_I(\mathbf{x})\, \mathbf{H}^{\mathrm{T}}(\mathbf{x}_I) = \mathbf{H}^{\mathrm{T}}(\mathbf{x}) \quad \text{or} \quad \sum_{I=1}^{NP} N_I(\mathbf{x})\, \mathbf{H}^{\mathrm{T}}(\mathbf{x} - \mathbf{x}_I) = \mathbf{H}^{\mathrm{T}}(\mathbf{0}) \tag{22}$$

which leads to $\mathbf{b}(\mathbf{x})$ of the following form:

$$\mathbf{b}^{\mathrm{T}}(\mathbf{x}) = \mathbf{H}^{\mathrm{T}}(\mathbf{0}) \mathbf{M}^{-1}(\mathbf{x}) \tag{23}$$

where the moment matrix is defined as

$$\mathbf{M}(\mathbf{x}) = \sum_{I=1}^{NP} \mathbf{H}(\mathbf{x} - \mathbf{x}_I) \mathbf{H}^{\mathrm{T}}(\mathbf{x} - \mathbf{x}_I) \Phi_a(\mathbf{x} - \mathbf{x}_I) \tag{24}$$

Combining Eqs. (18), (20) and (23), the reproducing kernel shape function is obtained as

$$N_I(\mathbf{x}) = \mathbf{H}^{\mathrm{T}}(\mathbf{0}) \mathbf{M}^{-1}(\mathbf{x}) \mathbf{H}(\mathbf{x} - \mathbf{x}_I) \Phi_a(\mathbf{x} - \mathbf{x}_I) \tag{25}$$

3.2. Reproducing kernel u–p approximation and discretization

Applying the reproducing kernel approximation to both the trial and test functions for the solid displacement and fluid pressure, we have

$$\mathbf{u}^h = \mathbf{N}^u \mathbf{U}, \quad p^h = \mathbf{N}^p \mathbf{P} \tag{26}$$

$$\boldsymbol{\eta}^h = \mathbf{N}^u \mathbf{c}^u, \quad \psi^h = \mathbf{N}^p \mathbf{c}^p \tag{27}$$

where $\mathbf{N}^u$ and $\mathbf{N}^p$ are the matrices of reproducing kernel shape functions using linear basis for displacement and pressure fields, respectively, and $\mathbf{U}$, $\mathbf{P}$, $\mathbf{c}^u$ and $\mathbf{c}^p$ are vectors containing the corresponding nodal coefficients. Substituting the approximation functions into Eqs. (15) and (16), the following semi-discrete equations are obtained:

$$\begin{aligned}\mathscr{L}_1\left(\boldsymbol{\eta}^h; \mathbf{u}^h, p^h\right) \equiv & \int_\Omega \left(\nabla^s \boldsymbol{\eta}^h : \boldsymbol{\sigma}'' - \alpha p^h \nabla \cdot \boldsymbol{\eta}^h\right) \mathrm{d}\mathbf{x} \\ & - \int_{\Gamma_t} \boldsymbol{\eta}^h \cdot \bar{\mathbf{t}} \mathrm{d}\mathbf{s} - \int_\Omega \boldsymbol{\eta}^h \cdot \rho \mathbf{g} \mathrm{d}\mathbf{x} = 0\end{aligned} \tag{28}$$

$$\begin{aligned}L_2\left(\psi^h; \mathbf{u}^h, p^h\right) \equiv & \int_\Omega \alpha \psi^h \nabla \cdot \frac{\partial \mathbf{u}^h}{\partial t} \mathrm{d}\mathbf{x} + \int_\Omega \psi^h \frac{1}{Q} \frac{\partial p^h}{\partial t} \mathrm{d}\mathbf{x} \\ & + \int_\Omega \nabla \psi^h \cdot \mathbf{k}_f \cdot \nabla p^h \mathrm{d}\mathbf{x} + \int_{\Gamma_q} \psi^h \mathbf{n}_\Gamma \cdot \bar{\mathbf{q}}_f \mathrm{d}\mathbf{s} = 0\end{aligned} \tag{29}$$

which leads to the following system of coupled equations:

$$\mathbf{K}_{uu} \mathbf{U} - \mathbf{K}_{up} \mathbf{P} - \mathbf{F}^{ext} = \mathbf{0} \tag{30}$$

$$\mathbf{K}_{up}^{\mathrm{T}} \frac{\partial \mathbf{U}}{\partial t} + \mathbf{K}_{pp}^{(S)} \frac{\partial \mathbf{P}}{\partial t} + \mathbf{K}_{pp}^{(H)} \mathbf{P} - \mathbf{Q}^{ext} = \mathbf{0} \tag{31}$$

where the matrices and vectors can be expressed as follows:

$$\text{Solid stiffness matrix} \quad \mathbf{K}_{uu} = \int_\Omega \mathbf{B}^{u\mathrm{T}}\mathbf{D}\mathbf{B}^u \mathrm{d}\mathbf{x} \tag{32}$$

$$\text{Coupling matrix} \quad \mathbf{K}_{up} = \int_\Omega \mathbf{B}^{u\mathrm{T}}\alpha\mathbf{m}\mathbf{N}^p \mathrm{d}\mathbf{x}, \tag{33}$$

$$\text{Compressibility matrix} \quad \mathbf{K}_{pp}^{(S)} = \int_\Omega \mathbf{N}^{p\mathrm{T}} Q^{-1}\mathbf{N}^p \mathrm{d}\mathbf{x} \tag{34}$$

$$\text{Permeability matrix} \quad \mathbf{K}_{pp}^{(H)} = \int_\Omega \mathbf{B}^{p\mathrm{T}}\mathbf{k}_f\mathbf{B}^p \mathrm{d}\mathbf{x} \tag{35}$$

$$\text{External force vector} \quad \mathbf{F}^{ext} = \int_{\Gamma_t} \mathbf{N}^{u\mathrm{T}}\bar{\mathbf{t}}\mathrm{d}\mathbf{s} + \int_\Omega \mathbf{N}^{u\mathrm{T}}\rho\mathbf{g}\mathrm{d}\mathbf{x} \tag{36}$$

$$\text{External flow flux vector} \quad \mathbf{Q}^{ext} = -\int_{\Gamma_q} \mathbf{N}^{p\mathrm{T}}\mathbf{n}_\Gamma \cdot \bar{\mathbf{q}}_f \mathrm{d}\mathbf{s} \tag{37}$$

In the above equations, $\mathbf{B}^u$ and $\mathbf{B}^p$ are the standard gradient matrices associated with the displacement and pressure approximation fields, respectively, $\mathbf{D}$ is the matrix form of elastic material constants in the constitutive tensor $\mathbf{C}$, and $\mathbf{m} = [1 \quad 1 \quad 0]^T$ in Eq. (33).

3.3. Discrete equations

The backward Euler method is employed which ensures unconditional stability in the temporal discretization. If the problem is to be solved between an initial time t_0 and a final time t_f, a partition of the time interval is considered, resulting in a series of time increments $\Delta t_{n+1} = t_{n+1} - t_n$. Evaluating the semi-discrete Eqs. (30) and (31) at time t_{n+1} and applying the following time marching scheme:

$$\left.\frac{\partial(\cdot)}{\partial t}\right|_{t_{n+1}} \cong \frac{\Delta(\cdot)_{n+1}}{\Delta t_{n+1}} = \frac{(\cdot)_{n+1} - (\cdot)_n}{\Delta t_{n+1}} \tag{38}$$

then the full discrete equations can be expressed as

$$\mathbf{K}_{uu}\mathbf{U}_{n+1} - \mathbf{K}_{up}\mathbf{P}_{n+1} - \mathbf{F}_{n+1}^{ext} = \mathbf{0} \tag{39}$$

$$\mathbf{K}_{up}^{\mathrm{T}}\Delta\mathbf{U}_{n+1} + \mathbf{K}_{pp}^{(S)}\Delta\mathbf{P}_{n+1} + \Delta t\mathbf{K}_{pp}^{(H)}\mathbf{P}_{n+1} - \Delta t\mathbf{Q}_{n+1}^{ext} = \mathbf{0} \tag{40}$$

Finally, we obtain the following system of equations to solve at every time step:

$$\mathbf{J}_{n+1}\mathbf{X}_{n+1} = \mathbf{R}_{n+1} \tag{41}$$

where

$$\mathbf{X}_{n+1} = \begin{pmatrix}\mathbf{U}_{n+1}\\ \mathbf{P}_{n+1}\end{pmatrix} \tag{42}$$

$$\mathbf{J}_{n+1} = \begin{bmatrix}\mathbf{K}_{uu} & -\mathbf{K}_{up}\\ -\mathbf{K}_{up}^{\mathrm{T}} & -\mathbf{K}_{pp}^{(S)} - \Delta t_{n+1}\mathbf{K}_{pp}^{(H)}\end{bmatrix} \tag{43}$$

$$\mathbf{R}_{n+1} = \begin{bmatrix}\mathbf{0} & \mathbf{0}\\ -\mathbf{K}_{up}^{\mathrm{T}} & -\mathbf{K}_{pp}^{(S)}\end{bmatrix}\begin{pmatrix}\mathbf{U}_n\\ \mathbf{P}_n\end{pmatrix} + \begin{pmatrix}\mathbf{F}_{n+1}^{ext}\\ -\Delta t\mathbf{Q}_{n+1}^{ext}\end{pmatrix} \tag{44}$$

In the present study, the monolithic solution strategy is adopted by which the primary unknowns of the fully coupled equations are solved simultaneously. Alternatively, a staggered or sequential coupling scheme can be used, and then a relatively small system of equations is solved at each time before sharing its information with other solvers through iteration. However, unlike the monolithic scheme, it is non-trivial to fully capture the coupling effects by using staggered solvers and also convergence difficulties may be encountered unless special techniques are utilized [20,48].

4. Fluid pressure projection for meshfree method with nodal integration

4.1. Pressure projection

When an equal-order approximation pair is adopted in the Bubnov–Galerkin approximation of the coupled problem described in previous sections, non-physical spatial oscillations can occur in the fluid pressure field when the porous medium is under nearly impermeable or undrained conditions. This problem is due to violation of the following discrete inf-sup condition [21–23]:

$$\sup_{\mathbf{u}^h \in S_u^h} \frac{\int_\Omega p^h \nabla\cdot\mathbf{u}^h \mathrm{d}\mathbf{x}}{\left\|\mathbf{u}^h\right\|_1} \geq C_0 \left\|p^h\right\|_0 \qquad \forall p^h \in S_p^h \tag{45}$$

where C_0 is a positive constant independent of the numerical discretization. However, it has been found that equal-order approximation pairs indeed satisfy a weaker inf-sup condition [31,32] expressed by

$$\sup_{\mathbf{u}^h \in S_u^h} \frac{\int_\Omega p^h \nabla\cdot\mathbf{u}^h \mathrm{d}\mathbf{x}}{\left\|\mathbf{u}^h\right\|_1} + \sum_{\Omega_I\in\Omega} C_1 \left\|p^h - \Pi p^h\right\|_{0,\Omega_I} \geq C_2 \left\|p^h\right\|_0 \qquad \forall p^h \in S_p^h \tag{46}$$

where C_1 and C_2 are positive constants independent of the numerical discretization; Ω_I is a sub-domain associated with the spatial discretization, for example, it can be represented by an element domain in the finite element context; Πp^h is the L_2 projection of the fluid pressure approximation field onto a lower-order space by minimizing the following functional:

$$\Theta\left(\Pi p^h\right)\big|_{\Omega_I} = \left\|p^h - \Pi p^h\right\|^2_{L_2(\Omega_I)} \tag{47}$$

For a linear approximation of the fluid pressure, we perform the projection to a constant field to yield

$$\Pi p^h\big|_{\Omega_I} = \frac{1}{V_I}\int_{\Omega_I} p^h \mathrm{d}\mathbf{x} \tag{48}$$

where V_I refers to the volume of the domain Ω_I in 3D or the area in 2D. Comparing Eqs. (45) and (46), it can be observed that the term $C_1\|p^h - \Pi p^h\|_{0,\Omega_I}$can remedy the inherent deficiency in the equal-order approximation pair. Based on this analogy, White and Borja [31] proposed to include a stabilization term to the bilinear finite element formulation in order to eliminate the spurious fluid pressure oscillation modes. Later, the finite element formulation using this fluid pressure projection method was further developed for large deformation poromechanical simulations [32], thermo-hydro-mechanical simulations [33] and the modeling of porous media with double porosity [34]. Similar schemes have previously been developed for stabilizing the numerical solutions of the Stokes equations [38,39], and for nearly incompressible elasticity problems [35–37]. Along this line, the fluid pressure projection method is employed in the present study for the meshfree formulation for coupled poromechanics problems within the stabilized conforming nodal integration framework. As mentioned, an additional stabilization term is added to the variational Eq. (29) to correct the deficiency of the equal-order u–p approximation, leading to the following stabilized variational equation

$$\mathscr{L}_2^h\left(\psi^h; \mathbf{u}^h, p^h\right) \equiv \mathscr{L}_2^h\left(\psi^h; \mathbf{u}^h, p^h\right) + \int_\Omega \varepsilon_f\left(\psi^h - \Pi\psi^h\right)\frac{\partial}{\partial t}\left(p^h - \Pi p^h\right)\mathrm{d}\mathbf{x} = 0 \tag{49}$$

Since the reproducing kernel approximation is purely based on nodal information, i.e., there is no element domain as in the FEM context, a suitable L_2 projection operator needs to be defined. To be compatible with the stabilized conforming nodal integration (SCNI) framework to be described in the next section, we choose the SCNI nodal representative integration domain as the subdomain Ω_I used for the operator Π. Following the same descritization procedure as introduced in previous sections, we can obtain the stabilized system of discrete equations at time step n:

$$\bar{\mathbf{J}}_{n+1}\mathbf{X}_{n+1} = \bar{\mathbf{R}}_{n+1} \tag{50}$$

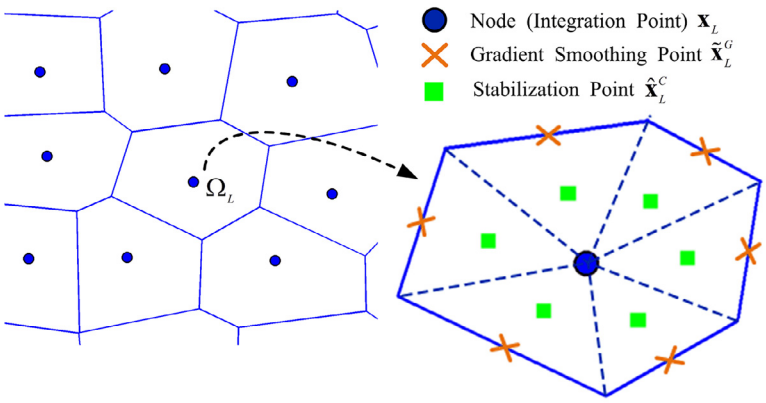

Fig. 2. Nodal representative domain for stabilized conforming nodal integration (SCNI) and fluid pressure projection (FPP).

where

$$\bar{\mathbf{J}}_{n+1} = \begin{bmatrix} \mathbf{K}_{uu} & -\mathbf{K}_{up} \\ -\mathbf{K}_{up}^{\mathrm{T}} & -\mathbf{K}_{pp}^{(S)} - \Delta t_{n+1}\mathbf{K}_{pp}^{(H)} - \mathbf{S} \end{bmatrix} \tag{51}$$

$$\bar{\mathbf{R}}_{n+1} = \begin{bmatrix} \mathbf{0} & \mathbf{0} \\ -\mathbf{K}_{up}^{\mathrm{T}} & -\mathbf{K}_{pp}^{(S)} - \mathbf{S} \end{bmatrix} \begin{pmatrix} \mathbf{U}_n \\ \mathbf{P}_n \end{pmatrix} + \begin{pmatrix} \mathbf{F}_{n+1}^{ext} \\ -\Delta t \mathbf{Q}_{n+1}^{ext} \end{pmatrix} \tag{52}$$

$$\mathbf{S} = \int_\Omega \varepsilon_f [\mathbf{N}^p - \Pi \mathbf{N}^p]^{\mathrm{T}} [\mathbf{N}^p - \Pi \mathbf{N}^p] \mathrm{d}\mathbf{x} \tag{53}$$

As can be seen, the fluid pressure projection based stabilization only requires modification of the p–p block of the Jacobian and the right hand side of the discrete equations with a symmetric matrix $\mathbf{S}$, and no stress-recovery techniques or second-order derivatives of the shape functions are needed as in the Petrov–Galerkin based stabilization approaches [20,29], and also the stability property of the time-integration scheme is not affected, unlike the fractional step algorithm [27,28]. An estimation of the stabilization parameter ε_f following Sun et al. [32] is given as follows:

$$\varepsilon_f = \frac{1}{M'} \left\langle 1 - 3\frac{c_v \Delta t}{h^2} \right\rangle \left(1 + \tanh\left(2 - 12\frac{c_v \Delta t}{h^2} \right) \right) \tag{54}$$

where

$$c_v = k_f M' = \frac{k_f (K + 4G/3)}{(K + 4G/3)/M_B + \alpha^2} \tag{55}$$

in which $\langle \cdot \rangle$ is the Macaulay bracket, and the Biot modulus is defined as $M_B = K_s K_f / [K_f(\alpha - n_f) + K_s n_f]$, k_f is the permeability parameter, α is Biot's coefficient, n_f is the porosity, G is the shear modulus, K, K_s and K_f are the averaged bulk modulus of the solid skeleton, solid grains and fluid, respectively, as defined in Section 2.1, and h is a characteristic length depending on the numerical discretization, for which we adopt a simple definition as $h = \sqrt{A_I}$ for two dimensional problem, where A_I is the area of the representative domain of node I as discussed in next section. It can be seen from Eq. (54), as the permeability becomes high, the parameter ε_f will approach to zero by construction, therefore over diffusion due to stabilization would be avoided automatically. This property of the adopted stabilization parameter makes the projection method suitable for solving problems under different drainage conditions, as to be shown in the numerical examples in Section 5.

4.2. Stabilized conforming nodal integration for pressure projection

The domain integration for the discrete equations introduced previously can be performed by using the Gauss integration method. However, in order to obtain accurate, convergent solutions, expensive high order Gauss integration is required. Stabilized conforming nodal integration method, on the other hand, achieves high accuracy and optimal convergence, and is also computationally efficient [42,43]. In this method, shape function gradients are smoothed over conforming nodal representative domains, and domain integration is performed at each node. The smoothed gradient of the shape functions are defined as

$$\tilde{\nabla} N_I(\mathbf{x}_L) \equiv \frac{1}{A_L} \int_{\Omega_L} \nabla N_I(\mathbf{x}) \mathrm{d}\mathbf{x} = \frac{1}{A_L} \int_{\Gamma_L} N_I(\mathbf{x}) \mathbf{n}(\mathbf{x}) \mathrm{d}\mathbf{s} \cong \frac{1}{A_L} \sum_{G=1}^{NG} N_I(\tilde{\mathbf{x}}_L^G) \mathbf{n}(\tilde{\mathbf{x}}_L^G) l_G \tag{56}$$

where $\tilde{\nabla}$ is the smoothed gradient operator and $\tilde{\nabla} N_I(\mathbf{x}_L)$ denotes the smoothed $\nabla N_I(\mathbf{x})$ associated with nodal point $\mathbf{x}_L$, Γ_L and Γ_G refer to the whole boundary and the G^{th} boundary segment of the nodal representative domain Ω_L, respectively, $A_L = \int_{\Omega_L} \mathrm{d}\mathbf{x}$, $l_G = \int_{\Gamma_G} \mathrm{d}\mathbf{s}$, $\mathbf{n}(\mathbf{x})$ is the outer unit normal to Γ_L, and NG is the total number of gradient smoothing evaluation points $\tilde{\mathbf{x}}_L^G$ which rest at the centroids of the boundary segments. The nodal representative domains can be constructed by Delaunay triangulation or Voronoi diagram, as shown in Fig. 2.

SCNI avoids rank deficiency in direct nodal integration, however spurious low-energy modes may still appear in the solution. Puso and Chen et al. [49] proposed to use more 'stress points' for stabilization which leads to the following expressions of Eqs. (32–35) and (53) as a stabilized nodal integration:

$$[\mathbf{K}_{uu}]_{IJ} = \int_\Omega \mathbf{B}_I^{u\mathrm{T}} \mathbf{D} \mathbf{B}_J^u \mathrm{d}\mathbf{x} \cong \sum_{L=1}^{NP} \left\{ \tilde{\mathbf{B}}_I^{u\mathrm{T}}(\mathbf{x}_L) \mathbf{D} \tilde{\mathbf{B}}_J^u(\mathbf{x}_L) A_L + \varepsilon_p \sum_{C \in T_L} \left[\tilde{\mathbf{B}}_I^u(\mathbf{x}_L) - \tilde{\mathbf{B}}_I^u(\hat{\mathbf{x}}_L^C) \right]^{\mathrm{T}} \mathbf{D} \left[\tilde{\mathbf{B}}_J^u(\mathbf{x}_L) - \tilde{\mathbf{B}}_J^u(\hat{\mathbf{x}}_L^C) \right] A_C \right\} \tag{57}$$

$$[\mathbf{K}_{up}]_{IJ} = \int_\Omega \mathbf{B}_I^{u\mathrm{T}} \alpha \mathbf{m} \mathbf{N}_J^p \mathrm{d}\mathbf{x} \cong \sum_{L=1}^{NP} \tilde{\mathbf{B}}_I^{u\mathrm{T}}(\mathbf{x}_L) \alpha \mathbf{m} \mathbf{N}_J^p(\mathbf{x}_L) A_L \tag{58}$$

$$\left[\mathbf{K}_{pp}^{(S)}\right]_{IJ} = \int_\Omega \mathbf{N}_I^{p\mathrm{T}} Q^{-1} \mathbf{N}_J^p \mathrm{d}\mathbf{x} \cong \sum_{L=1}^{NP} \left\{ \mathbf{N}_I^{p\mathrm{T}}(\mathbf{x}_L) Q^{-1} \mathbf{N}_J^p(\mathbf{x}_L) A_L + \varepsilon_p \sum_{C \in T_L} \left[\mathbf{N}_I^p(\mathbf{x}_L) - \mathbf{N}_J^p(\hat{\mathbf{x}}_L^C) \right]^{\mathrm{T}} Q^{-1} \left[\mathbf{N}_I^p(\mathbf{x}_L) - \mathbf{N}_J^p(\hat{\mathbf{x}}_L^C) \right] A_C \right\} \tag{59}$$

$$\left[\mathbf{K}_{pp}^{(H)}\right]_{IJ} = \int_{\Omega} \mathbf{B}_I^{pT}\mathbf{k}_f\mathbf{B}_J^p \mathrm{d}\mathbf{x} \cong \sum_{L=1}^{NP}\left\{\tilde{\mathbf{B}}_I^{pT}(\mathbf{x}_L)\mathbf{k}_f\tilde{\mathbf{B}}_J^p(\mathbf{x}_L)A_L + \varepsilon_p \sum_{C\in T_L}\left[\tilde{\mathbf{B}}_I^p(\mathbf{x}_L) - \tilde{\mathbf{B}}_I^p\left(\hat{\mathbf{x}}_L^C\right)\right]^{\mathrm{T}}\mathbf{k}_f\left[\tilde{\mathbf{B}}_J^p(\mathbf{x}_L) - \tilde{\mathbf{B}}_J^p\left(\hat{\mathbf{x}}_L^C\right)\right]A_C\right\} \tag{60}$$

$$[\mathbf{S}]_{IJ} = \int_{\Omega} \varepsilon_f[\mathbf{N}_I^p - \Pi\mathbf{N}_I^p]^{\mathrm{T}}[\mathbf{N}_J^p - \Pi\mathbf{N}_J^p]\mathrm{d}\mathbf{x} \cong \sum_{L=1}^{NP}\left\{\varepsilon_f(\mathbf{x}_L)[\mathbf{N}_I^p(\mathbf{x}_L) - \Pi\mathbf{N}_I^p(\mathbf{x}_L)]^{\mathrm{T}}[\mathbf{N}_J^p(\mathbf{x}_L) - \Pi\mathbf{N}_J^p(\mathbf{x}_L)]A_L + \varepsilon_p\varepsilon_f(\mathbf{x}_L)\sum_{C\in T_L}[\mathbf{N}_I^p(\mathbf{x}_L) - \Pi\mathbf{N}_I^p(\hat{\mathbf{x}}_L^C)]^{\mathrm{T}}[\mathbf{N}_J^p(\mathbf{x}_L) - \Pi\mathbf{N}_J^p(\hat{\mathbf{x}}_L^C)]A_C\right\} \tag{61}$$

where $\tilde{\mathbf{B}}_I^u$ and $\tilde{\mathbf{B}}_I^p$ are the smoothed gradient matrices associated with $\tilde{\nabla}N_I$, T_L is the set of subcells C associated with each node L, A_C is the area of the C^{th} subcell which satisfies $A_L = \sum_{C\in T_L} A_C$, and the stabilization points $\hat{\mathbf{x}}_L^C$ rest at the centroids of the subcells as shown in Fig. 2. The expressions in Eqs. (57–61) are considered to be of the nodal integration type since material parameters and state variables are calculated and stored at the nodal points $\mathbf{x}_L$ only. Compared to direct nodal integration, the minor extra effort required in SCNI is to compute the shape functions and their smoothed gradients at a few stabilization points. The stabilization parameter $\varepsilon_p = 1$ is used in all the numerical examples in present study, as suggested by Puso and Chen et al. [49].

Furthermore, recalling the L_2 projection operator Π defined in Eq. (48), we can see that all the pressure projection terms appearing in Eq. (61) indeed can be computed within the same nodal integration framework in a straightforward way:

$$\Pi\mathbf{N}_I^p(\mathbf{x}_L) = \frac{1}{A_L}\int_{\Omega_L}\mathbf{N}_I^p\mathrm{d}\mathbf{x} \cong \frac{1}{A_L}\sum_{C\in T_L}\mathbf{N}_I^p\left(\hat{\mathbf{x}}_L^C\right)A_C \tag{62}$$

$$\Pi\mathbf{N}_I^p\left(\hat{\mathbf{x}}_L^C\right) = \frac{1}{A_C}\int_{\Omega_C}\mathbf{N}_I^p\mathrm{d}\mathbf{x} \cong \mathbf{N}_I^p\left(\hat{\mathbf{x}}_L^C\right) \tag{63}$$

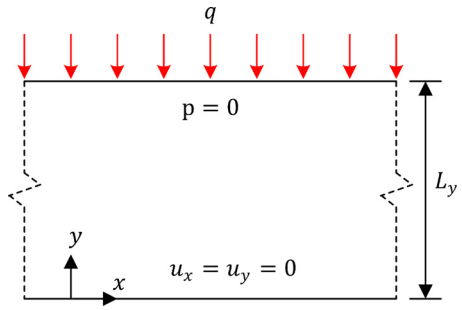

Fig. 3. Description of Terzaghi's problem.

which shows that shape functions evaluated at stabilization points can be used for both the fluid pressure projection and the stabilized nodal integration, saving computational cost. Since the evaluation of the pressure projection terms in Eqs. (62) and (63) already provides most of the matrices required for the evaluation of direct shape function derivatives, the smoothed gradients at the stabilization points in Eqs. (57) and (60) can be replaced with the direct gradients to reduce the number of gradient smoothing points. Consider that if a rectangular nodal integration domain is used for 2D problems, with SCNI the shape functions need to be evaluated at only 9 points, including the node itself, 4 stabilization points, and 4 gradient smoothing evaluation points. On the other hand, in order to achieve comparable accuracy with Gauss quadrature, both shape functions and their direct derivatives are required to be evaluated at 25 integration points at least [45]. The advantage of SCNI is more obvious in 3D applications, where 125 evaluation points are needed for Gauss quadrature using the commonly adopted hexahedron zones, while in the proposed nodal integration scheme the shape function evaluation is required at only 13 points, including the node itself, 6 stabilization points, and 6 gradient smoothing evaluation points. Clearly, the stabilized nodally integrated meshfree method is quite attractive for solving large-scale, coupled problems because of its high efficiency and accuracy.

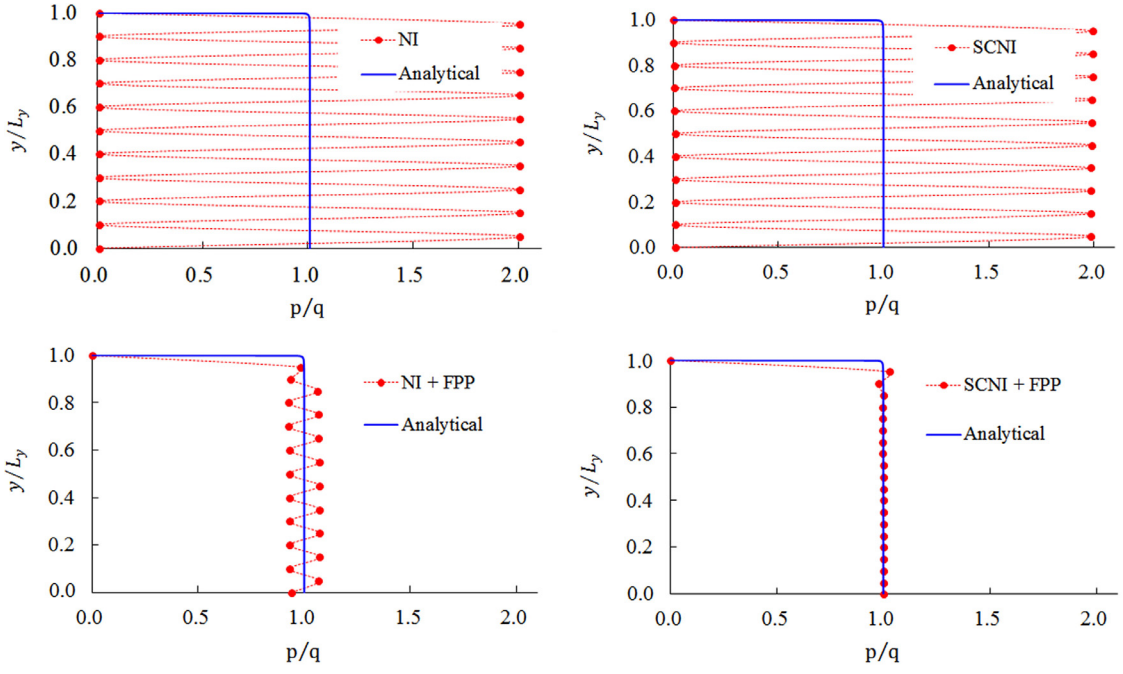

Fig. 4. Normalized fluid pressure profile for Terzaghi's problem.

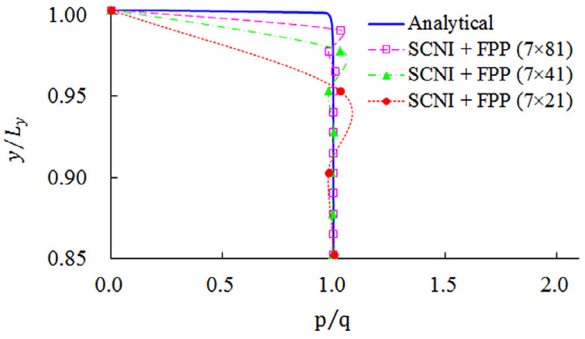

Fig. 5. Normalized fluid pressure profile near the drainage boundary.

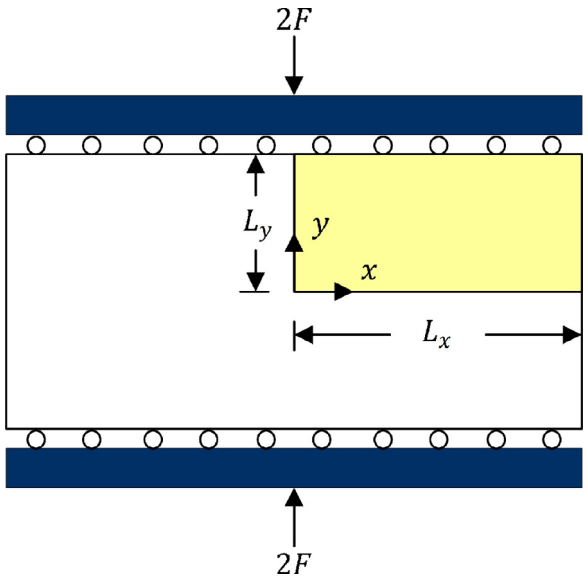

Fig. 6. Description of Mandel's problem. (For interpretation of the references to color in this figure, the reader is referred to the web version of this article).

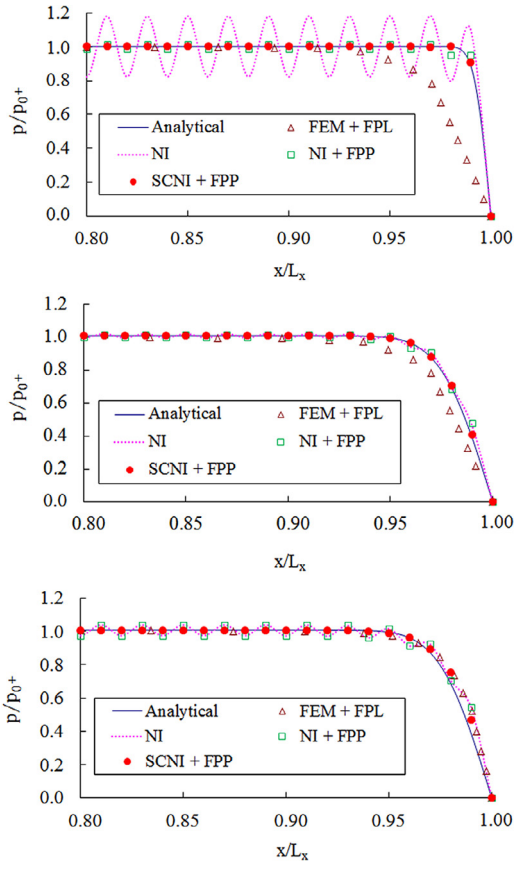

Fig. 7. Normalized fluid pressure distribution at time $T_D = 2.0 \times 10^{-5}$ using $\Delta t_D = 0.01$ with 20 time steps (top); at $T_D = 2.0 \times 10^{-4}$ using $\Delta t_D = 0.1$ with 20 time steps (middle) and using $\Delta t_D = 1.0$ with 2 time steps (bottom).

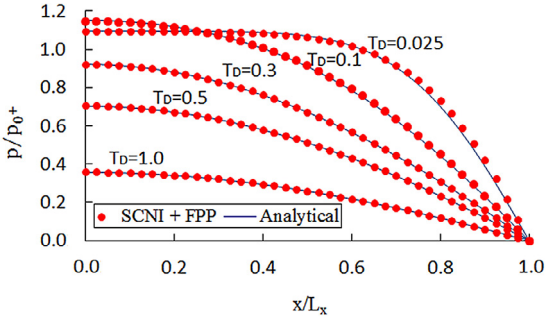

Fig. 8. Normalized fluid pressure distribution for Mandel's problem at various dimensionless time T_D.

5. Numerical examples

To verify the proposed formulation, several hydro-mechanical coupled problems are analyzed. For simplicity, the effect of gravity force is neglected, and as commonly adopted in soil mechanics the bulk modulus of the porous matrix is assumed to be much smaller than the bulk modulus of the grains, which is not a restriction of the present formulation. Linear basis is used for both the solid displacement and the fluid pressure fields, and the support size of the meshfree shape function is set to be 1.5 times the average nodal distance. Although meshfree shape functions do not have the Kronecker delta property, efficient treatments are available for the imposition of essential boundary conditions, such as Nistche's method, Lagrange multipliers, penalty method, the singular kernel method and transformation method, etc. [50,51]. In solving the following problems, both the penalty method and the transformation method have been tested and no noticeable difference in their results was found.

In the following, the fluid pressure projection approach is denoted as FPP, and NI refers to the direct nodal integration method, whereas SCNI denotes the stabilized conforming nodal integration method.

5.1. Terzaghi's problem

In the first numerical test, the classical Terzaghi's consolidation problem [52] is analyzed. As shown in Fig. 3, a soil layer of thickness $L_y = 10.0$ m is considered to be infinitely long in the horizontal direction. At initial time, a distributed load of constant intensity q is suddenly applied which expels the pore water from the top surface. A two dimensional numerical model for the domain size 3.0×10.0 m^2 is used, where the horizontal displacement at the boundary is fixed. The adopted time step is $\Delta t = 1.0$ s and the material parameters are chosen as follows: Young's modulus $E = 1.0$ kPa, Poisson's ratio $\nu = 0.0$, hydraulic conductivity $k_h = 1.0 \times 10^{-5}$ m/s, specific weight of fluid $\gamma_f = 10.0$ kN/m^3, and fluid bulk modulus $K_f = 2.2$ GPa.

The fluid pressure profile after the initial time step is shown in Fig. 4, where 7×21 nodes are used for the different numerical formulations. It can be seen that formulations using only SCNI or NI yield severe oscillations in fluid pressure field since the requirement of inf-sup condition is not satisfied. Although this spurious oscillation can be partially alleviated by adding FPP to the NI formulation, unphysical pressure modes are still observable due to the instability caused by the direct nodal integration method. On the other hand, a stable

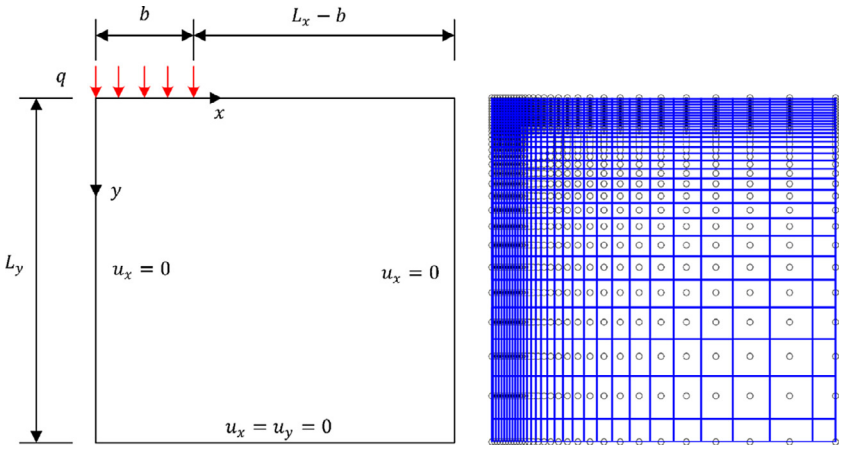

Fig. 9. Description of the footing problem (left) and its meshfree numerical model with the Voronoi diagram (right).

and accurate solution is obtained by employing FPP in conjunction with SCNI, achieving a good agreement with the analytical solution. Minor overshoot using the SCNI + FPP formulation appears near the drainage boundary, which is caused by the extremely sharp pressure gradient. This phenomenon is also observed in stable finite elements and would not affect the solution in the rest of the domain as discussed in [23,31]. Numerical results using 21, 41, and 81 nodes along the vertical direction are plotted in Fig. 5, showing that convergence can be achieved when the spatial discretization is refined.

5.2. Mandel's problem

As shown in Fig. 6, a pair of vertical loads of constant magnitude $2F$ is applied to a poroelastic soil sample through rigid and frictionless plates. The length and height of the rectangular soil sample are $2L_x$ and $2L_y$, respectively. While the two sides in lateral direction are fully drained, other boundaries are impermeable. Analytical expressions for the pressure and the vertical displacement fields are respectively derived by Mandel [53] and Abousleiman et al. [54] as follows:

$$p = 2p_{0^+}\sum_{n=1}^{\infty}\frac{\sin\alpha_n}{\alpha_n - \sin\alpha_n\cos\alpha_n}\left(\cos\frac{\alpha_n x}{L_x} - \cos\alpha_n\right)\exp\left(-\alpha_n^2 T_D\right)$$

$$u_y = \left[-\frac{(1-\nu)F}{2GL_x} + \frac{(1-\nu_u)F}{GL_x}\sum_{n=1}^{\infty}\frac{\sin\alpha_n\cos\alpha_n}{\alpha_n - \sin\alpha_n\cos\alpha_n}\exp\left(-\alpha_n^2 T_D\right)\right]y$$

where $T_D = c_f t/L_x^2$ is the dimensionless time, c_f is the fluid diffusivity coefficient, G is the shear modulus, α_n are the positive solutions to the nonlinear equation $(\tan\alpha_n)/\alpha_n = (1-\nu)/(\nu_u - \nu)$, in which $\nu_u = 0.5$ for incompressible fluid, and the fluid pressure distribution at the instant of loading $p_{0^+} \equiv \lim_{t\to 0} p$ depends on both the average force density $F/L_x$and material parameters, for which an analytical expression can be found in [54,55].

Considering the symmetries, only one quarter of the slab (i.e. the colored part in Fig. 6) is modeled with $L_x = 20.0$ and $L_y = 2.0$. Symmetric conditions are enforced on the left and the bottom boundaries, whereas vertical displacement on the top is controlled by applying the analytical solution using $F = 2L_x$. Initial conditions are set as zero for both displacement and fluid pressure fields. Incompressible fluid is assumed and material parameters are chosen from the reference [56] as $E = 1.0\times10^4$, $\nu = 0.0$, $\nu_u = 0.5$, $k_f = 1.0\times10^{-4}$, which results in $c_f = 1.0$ and $p_{0^+} = 1.0$.

The early time response of Mandel's problem has been analyzed by Preisig and Prevost [56] using stabilized FE formulation, for which three different dimensionless time increments $\Delta t_D = c_f\Delta t/h^2$ of 0.01, 0.1 and 1.0 are adopted, respectively, and their study shows that the undrained behavior could lead to spurious pressure oscillations in the numerical solution when small time increment is used and thus stabilization procedure is required. To assess the performance of the present meshfree formulation, the same dimensionless time increments are also chosen here. The meshfree computation results of the normalized fluid pressure distribution along horizontal direction using 101×11 nodes are given in Fig. 7 together with the analytical solutions and the stabilized finite element results from [56] denoted as FEM + FPL, where FPL denotes the fluid pressure Laplacian (FPL) stabilization method. It can be seen that oscillations appear for direct nodally integrated (NI) formulation even when FPP is applied, while the stable SCNI + FPP formulation can offer much satisfactory results compared with the reference solutions.

Next, the distribution of the fluid pressure for various time instants is plotted in Fig. 8. Again, good agreement is achieved between the analytical solutions and the SCNI + FPP meshfree formulation. An important aspect of Mandel's problem is that near the center

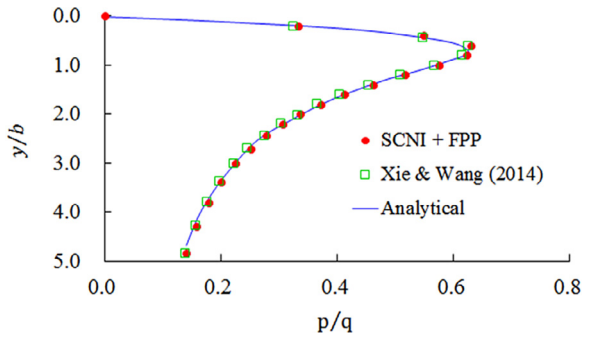

Fig. 10. Normalized fluid pressure distribution along the central vertical line at time $T_D = 0.1$.

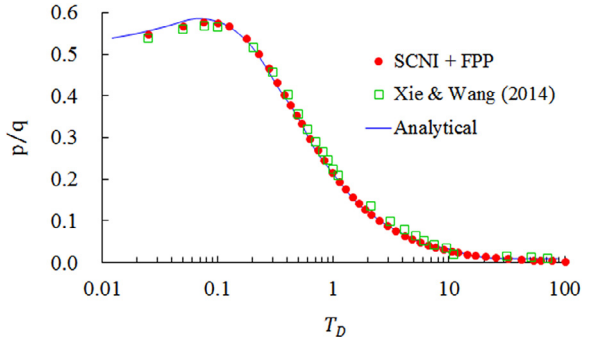

Fig. 11. Time history of fluid pressure at location $x = 0.0$m, $y = 0.2$m.

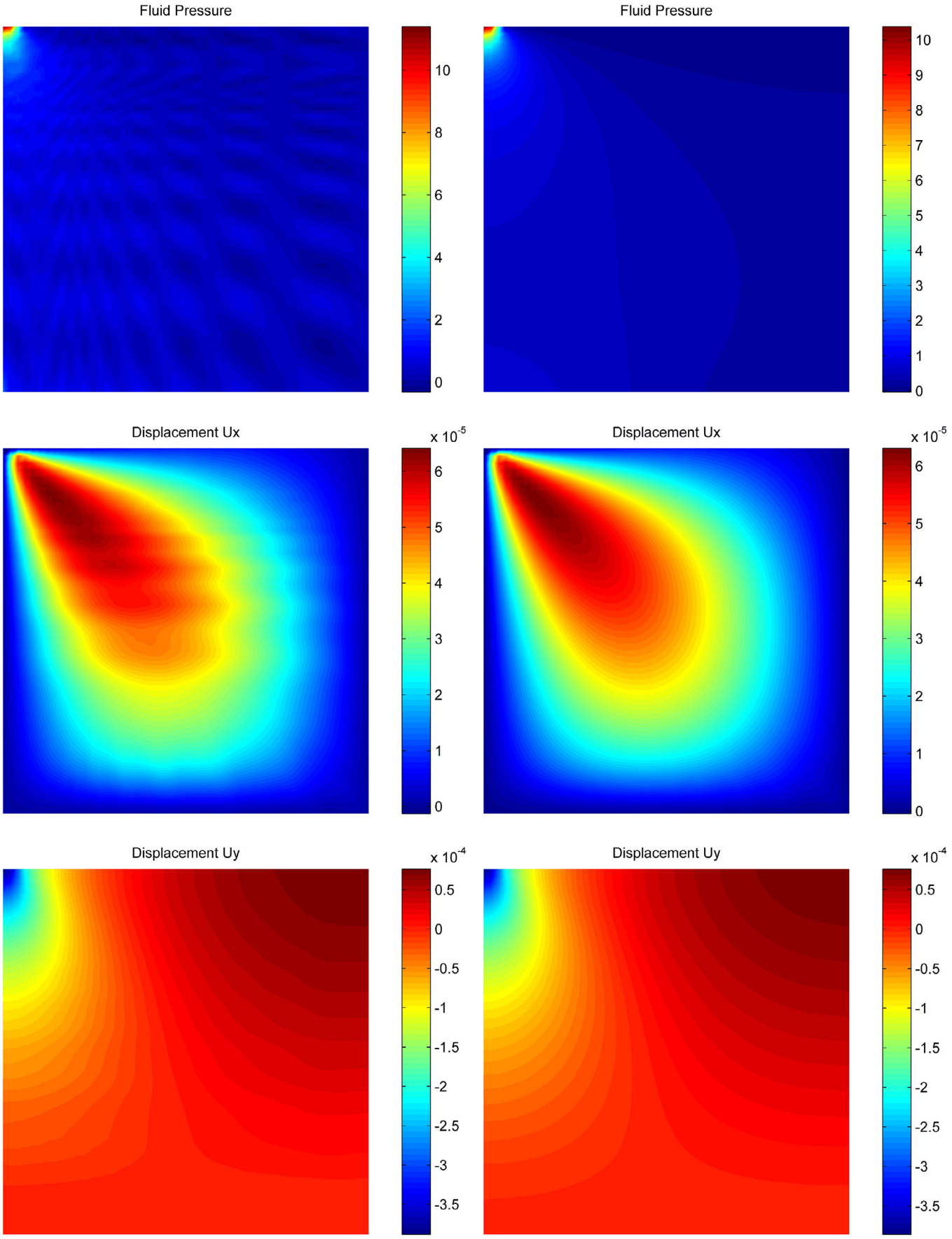

Fig. 12. Numerical results of the fluid pressure, horizontal displacement, and vertical displacement distribution (from top to bottom) for the low permeable case, using the NI formulation (left) and the SCNI+FPP formulation (right).

of the sample the pressure initially increases beyond the instantaneous response p_{0+} at time of loading, and it dissipates later, which is known as the Mandel–Cryer effect [53,57] due to the strong hydro-mechanical coupling and is confirmed by experiments [58]. As shown in Fig. 8, this coupling effect is well captured by the proposed stabilized meshfree formulation.

5.3. Strip load on elastic half space

A constant surface pressure of intensity $q = 10.0$kPa is distributed over a width of $2b = 0.4$m on the draining surface of the semi-infinite soil ground. The material parameters are as follows: Young's modulus $E = 1.0 \times 10^4$kPa, Poisson's ratio $\nu = 0.0$, hydraulic conductivity $k_h = 5.0 \times 10^{-8}$m/s, specific weight of fluid $\gamma_f = 9.8$kN/m^3, and the pore fluid is assumed to be incompressible. Due to symmetry, only one half of the domain is modeled, as shown in Fig. 9, where the height $L_x = 25b$ and width $L_y = 25b$ can be considered to be large enough to minimize the boundary effect in order to properly represent the infinite space.

This problem has been analyzed by Xie and Wang [20] using standard RKPM via a staggered strategy for solving the system of coupled equations, while here the same coupled equations are solved in a monolithic manner by applying the proposed stabilized, nodally integrated RKPM formulation. The same spatial discretization as that used in [20] is employed in this study, which consists of 31 $\times$ 31 non-uniformly distributed nodes. The adopted discretization is shown in Fig. 9 along with the nodal representative integration zones. For convenience, the dimensionless time is defined as $T_D = Ek_hT/(1+\nu)\gamma_f b^2$, and the time step size $\Delta t = 19.6$s is chosen such that the dimensionless time increment $\Delta t_D = Ek_h\Delta t/(1+\nu)\gamma_f b^2$is equal to 0.025.

The numerical results of pore fluid pressure at $x = 0.0$m along the height at $T_D = 0.1$ are plotted in Fig. 10, along with the analytical solution from [59,60]. As can be seen, good agreement between all the three results are obtained, which verifies the accuracy of the present approach. It should be noted that for the considered case no spurious pressure oscillations would appear even without FPP stabilization. The time history of the fluid pressure at location $x = 0.0$m, $y = 0.2$m is also plotted in Fig. 11 and again the proposed meshfree formulation gives satisfactory result.

To further demonstrate the robustness of the stabilized meshfree formulation, we analyze a low permeable case for which $k_h = 5.0 \times 10^{-13}$m/s is chosen and the surface boundary is treated as undrained. The spatial and temporal discretization is kept the same as before, and the numerical results using different formulations for the contours of fluid pressure and displacement fields are shown in Fig. 12. Clearly, severe oscillations appear in the fluid pressure field without using SCNI or FPP, which would also affect the horizontal displacement field although the vertical displacement field seems not to be influenced much. On the other hand, the proposed formulation (SCNI + FPP) gives a stable solution as expected.

6. Conclusions

A stable and efficient meshfree method is proposed to solve the fully coupled hydro-mechanical problems. It has been shown that the fluid pressure projection method can be naturally integrated within the stabilized conforming nodal integration framework, and thus the non-physical fluid pressure oscillation due to violation of the inf-sup condition as well as the spurious low-energy modes due to nodal integration can both be eliminated in a cost effective way. Several benchmark problems have been analyzed and the results demonstrate the excellent performance of the stabilized meshfree formulation. Although in the present study only two dimensional, linear problems are used as verification tests, the extension of this computational framework to three dimensional, non-linear problems is feasible, and the attractive features of the meshfree approximation method as discussed previously can be further exploited to model the hydro-mechanical coupled damage and fracture process with application to hydraulic fracturing simulation, which is an ongoing work and will be reported in our forthcoming paper.

Acknowledgments

The support from William Prager endowment of University of California, San Diego is gratefully acknowledged.

References

[1] Belytschko T, Lu YY, Gu L. Element-free Galerkin methods. Int J Numer Meth Eng 1994;37(2):229–56.
[2] Liu WK, Jun S, Zhang YF. Reproducing kernel particle methods. Int J Numer Meth Fluid 1995;20(8-9):1081–106.
[3] Chen JS, Pan C, Wu CT, Liu WK. Reproducing kernel particle methods for large deformation analysis of nonlinear structures. Comput Meth Appl Mech Eng 1996;139(1):195–227.
[4] Li S, Liu WK. Meshfree particle methods. Berlin, Heidelberg: Springer-Verlag; 2004.
[5] Belytschko T, Lu YY, Gu L, Tabbara M. Element-free Galerkin methods for static and dynamic fracture. Int J Solid Struct 1995;32(17):2547–70.
[6] Krysl P, Belytschko T. The element free Galerkin method for dynamic propagation of arbitrary 3-D cracks. Int J Numer Meth Eng 1999;44(6):767–800.
[7] Bordas S, Rabczuk T, Zi G. Three-dimensional crack initiation, propagation, branching and junction in non-linear materials by an extended meshfree method without asymptotic enrichment. Eng Fract Mech 2008;75(5):943–60.
[8] Chen JS, Wu CT, Belytschko T. Regularization of material instabilities by meshfree approximation with intrinsic length scales. Int J Numer Meth Eng 2000;47(7):1303–22.
[9] Chen JS, Zhang X, Belytschko T. An implicit gradient model by a reproducing kernel strain regularization in strain localization problems. Comput Meth Appl Mech Eng 2004;193(27):2827–44.
[10] Murakami A, Kawabata H, Aoyama S. EFGM analysis for saturated soil. In: Proceedings of the 10th international conference on computer methods and advances in geomechanics, Tucson; 2000.
[11] Karim MR, Nogami T, Wang JG. Analysis of transient response of saturated porous elastic soil under cyclic loading using element-free Galerkin method. Int J Solid Struct 2002;39(24):6011–33.
[12] Oliaei MN, Soga K, Pak A. Some numerical issues using element-free Galerkin mesh-less method for coupled hydromechanical problems. Int J Numer Anal Meth Geomech 2009;33(7):915–38.
[13] Shibata T, Murakami A. A stabilization procedure for soil-water coupled problems using the element-free Galerkin method. Comput Geotech 2011;38(5):585–97.
[14] Hua L. Stable element-free Galerkin solution procedures for the coupled soil-pore fluid problem. Int J Numer Meth Eng 2011;86(8):1000–26.
[15] Samimi S, Pak A. Three-dimensional simulation of fully coupled hydro-mechanical behavior of saturated porous media using element free Galerkin (EFG) method. Comput Geotech 2012;46:75–83.
[16] Wang JG, Liu GR, Wu YG. A point interpolation method for simulating dissipation process of consolidation. Comput Meth Appl Mech Eng 2001;190(45):5907–22.
[17] Wang JG, Liu GR, Lin P. Numerical analysis of Biot's consolidation process by radial point interpolation method. Int J Solid Struct 2002;39(6):1557–73.
[18] Khoshghalb A, Khalili N. A stable meshfree method for fully coupled flow-deformation analysis of saturated porous media. Comput Geotech 2010;37(6):789–95.
[19] Bui HH, Fukagawa R, Sako K, Ohno S. Lagrangian meshfree particles method (SPH) for large deformation and failure flows of geomaterial using elastic-plastic soil constitutive model. Int J Numer Anal Meth Geomech 2008;32(12):1537–70.
[20] Xie Y, Wang G. A stabilized iterative scheme for coupled hydro-mechanical systems using reproducing kernel particle method. Int J Numer Meth Eng 2014;99(11):819–43.
[21] Babuska I. The finite element method with Lagrange multipliers. Numer Math 1973;20:179–92.
[22] Brezzi F. On the existence, uniqueness and approximation of saddle-point problem arising from Lagrangian multipliers. ESAIM Math Model Numer Anal 1974;8(2):129–51.
[23] Haga JB, Osnes H, Langtangen HP. On the causes of pressure oscillations in low-permeable and low-compressible porous media. Int J Numer Anal Meth Geomech 2012;36(12):1507–22.
[24] Zienkiewicz OC, Chan AHC, Pastor M, Schrefler BA, Shiomi T. Computational geomechanics with special reference to earthquake engineering. New York: Wiley; 1999.
[25] Jha B, Juanes R. A locally conservative finite element framework for the simulation of coupled flow and reservoir geomechanics. Acta Geotech 2007;2(3):139–53.
[26] de Borst R, Rethore J, Abellan MA. A numerical approach for arbitrary cracks in a fluid-saturated medium. Arch Appl Mech 2006;75(10-12):595–606.
[27] Pastor M, Li T, Liu X, Zienkiewicz OC, Quecedo M. A fractional step algorithm allowing equal-order of interpolation for coupled analysis of saturated soil problems. Mech Cohes Frict Mater 2000;5(7):511–34.

[28] Li X, Han X, Pastor M. An iterative stabilized fractional step algorithm for finite element analysis in saturated soil dynamics. Comput Meth Appl Mech Eng 2003;192(35):3845–59.
[29] Wan J, Durlofsky LJ, Hughes TJR, Aziz K. Stabilized finite element methods for coupled geomechanics-reservoir flow simulations. In: Proceedings of SPE symposium on reservoir simulation, Houston; 2003.
[30] Truty A, Zimmermann T. Stabilized mixed finite element formulations for materially nonlinear partially saturated two-phase media. Comput Meth Appl Mech Eng 2006;195(13):1517–46.
[31] White JA, Borja RI. Stabilized low-order finite elements for coupled solid-deformation/fluid-diffusion and their application to fault zone transients. Comput Meth Appl Mech Eng 2008;197(49-50):4353–66.
[32] Sun WC, Ostien JT, Salinger AG. A stabilized assumed deformation gradient finite element formulation for strongly coupled poromechanical simulations at finite strain. Int J Numer Anal Meth Geomech 2013;37(16):2755–88.
[33] Sun WC. A stabilized finite element formulation for monolithic thermo-hydro-mechanical simulations at finite strain. Int J Numer Meth Eng 2015;103(11):798–839.
[34] Choo J, Borja RI. Stabilized mixed finite elements for deformable porous media with double porosity. Comput Meth Appl Mech Eng 2015;293:131–54.
[35] Chen JS, Pan C. A pressure projection method for nearly incompressible rubber hyperelasticity, part I: theory. J Appl Mech 1996;63(4):862–8.
[36] Chen JS, Wu CT, Pan C. A pressure projection method for nearly incompressible rubber hyperelasticity, part II: applications. J Appl Mech 1996;63(4):869–76.
[37] Chen JS, Yoon S, Wang HP, Liu WK. An improved reproducing kernel particle method for nearly incompressible finite elasticity. Comput Meth Appl Mech Eng 2000;181(1):117–45.
[38] Dohrmann CR, Bochev PB. A stabilized finite element method for the Stokes problem based on polynomial pressure projections. Int J Numer Meth Fluid 2004;46(2):183–201.
[39] Bochev PB, Dohrmann CR, Gunzburger MD. Stabilization of low-order mixed finite elements for the Stokes equations. SIAM J Numer Anal 2006;44(1):82–101.
[40] Dolbow J, Belytschko T. Numerical integration of Galerkin weak form in meshfree methods. Comput Mech 1999;23(3):219–30.
[41] Beissel S, Belytschko T. Nodal integration of the element-free Galerkin method. Comput Meth Appl Mech Eng 1996;139(1):49–74.
[42] Chen JS, Wu CT, Yoon S, You Y. A stabilized conforming nodal integration for Galerkin meshfree methods. Int J Numer Meth Eng 2001;50(2):435–66.
[43] Chen JS, Yoon S, Wu CT. Non-linear version of stabilized conforming nodal integration for Galerkin mesh-free methods. Int J Numer Meth Eng 2002;53(12):2587–615.
[44] Duan Q, Li X, Zhang H, Wang B, Gao X. Quadratically consistent one-point (QC1) quadrature for meshfree Galerkin methods. Comput Meth Appl Mech Eng 2012;245:256–72.
[45] Chen JS, Hillman M, Rüter M. An arbitrary order variationally consistent integration method for Galerkin meshfree methods. Int J Numer Meth Eng 2013;95(5):387–418.
[46] Biot MA. General theory of three-dimensional consolidation. J Appl Phys 1941;12(2):155–64.
[47] Coussy O. Poromechanics. New York: Wiley; 2004.
[48] Kim J, Tchelepi HA, Juanes R. Stability and convergence of sequential methods for coupled flow and geomechanics: fixed-stress and fixed-strain splits. Comput Meth Appl Mech Eng 2011;200(13):1591–606.
[49] Puso M, Chen JS, Zywick E, Elmer W. Meshfree and finite element nodal integration methods. Int J Numer Meth Eng 2008;74(3):416–46.
[50] Chen JS, Wang HP. New boundary condition treatments in meshfree computation of contact problems. Comput Meth Appl Mech Eng 2000;187(3):441–68.
[51] Fernández-Méndez S, Huerta A. Imposing essential boundary conditions in meshfree methods. Comput Meth Appl Mech Eng 2004;193(12):1257–75.
[52] Verruijt A, van Baars S (2007) Soil mechanics. VSSD: Delft.
[53] Mandel J. Consolidation des sols. Géotechnique 1953;3(7):287–99.
[54] Abousleiman Y, Cheng AHD, Cui L, Detournay E, Roegiers JC. Mandel's problem revisited. Géotechnique 1996;46(2):187–95.
[55] Phillips PJ, Wheeler MF. A coupling of mixed and continuous Galerkin finite element methods for poroelasticity I: the continuous in time case. Comput Geosci 2007;11(2):131–44.
[56] Preisig M, Prevost JH. Stabilization procedures in coupled poromechanics problems: a critical assessment. Int J Numer Anal Meth Geomech 2011;35(11):1207–25.
[57] Cryer CW. A comparison of the three-dimensional consolidation theories of Biot and Terzaghi. Q J Mech Appl Math 1963;16(3):401–12.
[58] Gibson RE, Knight K, Taylor PW. A critical experiment to examine theories of three-dimensional consolidation. In: Proceedings of the European conference on soil mechanics and foundation engineering, Wiesbaden; 1963.
[59] Chen ATF. Plane strain and axisymmetric primary consolidation of saturated clays, Troy, New York: Rensselaer Polytechnic Institute; 1966. [Ph.D. thesis].
[60] Schiffman RL, Chen ATF, Jordan JC. An analysis of consolidation theories. J Soil Mech Found Div 1969;95:285–312.